Environmental Technology & Innovation 43 (2026) 105120

Contents lists available at ScienceDirect

Environmental Technology & Innovation

journal homepage: www.elsevier.com/locate/eti

Electrospun cellulose acetate/g-C_3N_4 membranes as metal-free photocatalysts for visible-light-driven wastewater remediation

Edward Hermosilla [a,*], Ana Obreque [b], Jeyson Hermosilla [c,d], Pablo IR Pincheira [e], Andrés Quiroz [b,f], Francisca Acevedo [c,d,g], Marcela Diaz [b,h], María Cristina Diez [b], Olga Rubilar [b,h,**]

[a] Instituto de Ciencias Aplicadas, Facultad de Ingeniería, Universidad Autónoma de Chile, Temuco 4810101, Chile
[b] Centro de excelencia en Investigación Biotecnológica Aplicada al Medio Ambiente (CIBAMA), Universidad de La Frontera, Avenida Francisco Salazar, Casilla 54-D, Temuco 01145, Chile
[c] Center of Excellence in Translational Medicine (CEMT), Facultad de Medicina, Universidad de La Frontera, Avenida Alemania 0458, Temuco, and Scientific and Technological Bioresource Nucleus (BIOREN), Universidad de La Frontera, Avenida Francisco Salazar, Casilla 54-D, Temuco 01145, Chile
[d] Millennium Nucleus Bioproducts, Genomics and Environmental Microbiology (BioGEM), Avenida España 1680, Valparaíso 2390123 Chile
[e] Department of Mechanical Engineering, Universidad de La Frontera, Francisco Salazar 01145, Temuco 4780000, Chile
[f] Departamento de Ciencias Químicas y Recursos Naturales, Universidad de La Frontera, Casilla 54-D, Temuco 4811230, Chile
[g] Department of Basic Sciences, Faculty of Medicine, Universidad de La Frontera, Avenida Francisco Salazar, Casilla 54-D, Temuco 01145, Chile
[h] Departamento de Ingeniería Química, Universidad de La Frontera, Avenida Francisco Salazar, Casilla 54-D, Temuco, La Araucanía 01145, Chile

ARTICLE INFO

Keywords:
Graphitic carbon nitride
Electrospun nanofibers
Visible-light photocatalysis
Sustainable water remediation

ABSTRACT

Developing sustainable, metal-free photocatalytic systems for wastewater remediation remains challenging: powdered photocatalysts agglomerate in aqueous media, lose active surface area, and are difficult to recover. Herein, we report g-C_3N_4/cellulose acetate (CA) nanofibrous membranes fabricated via electrospinning as a solution for continuous water treatment, evaluated using methylene blue (MB) as a model probe. Graphitic carbon nitride (g-C_3N_4) nanosheets, characterized by a 2.73 eV band gap and a layered polymeric structure, were embedded into CA nanofibers to overcome these dispersibility and recovery barriers. FTIR shifts of the C═O and s-triazine modes revealed an interfacial interaction between g-C_3N_4 and the CA matrix, indicating intimate coupling rather than simple physical entrapment, while the electrospun architecture provided hierarchical porosity maximizing light harvesting and mass transfer. Scavenger assays identified superoxide radicals ($\bullet O_2^-$) as the primary reactive species, with a secondary contribution from singlet oxygen ($^1O_2$), consistent with a reductive oxygen-activation pathway imposed by the band structure of g-C_3N_4. Key achievements are: (i) a fully organic, metal-free membrane obtained by a single-step, scalable route; (ii) 98.7% MB degradation within 240 min under visible light ($k_{app} = 1.67 \times 10^{-2}$ min^{-1}), ~2-fold higher than pristine g-C_3N_4 and 1.5–14 times higher than phase-inversion CA membranes loaded with ZnO, TiO_2 or CeO_2; (iii) a 63% increase in dark MB uptake versus pristine CA, pre-concentrating the dye at catalytic sites; (iv) stable operation across a broad alkaline window (pH 8–10); and (v) solvent-free, light-driven regeneration preserving

* Corresponding author.
** Corresponding author at: Centro de excelencia en Investigación Biotecnológica Aplicada al Medio Ambiente (CIBAMA), Universidad de La Frontera, Avenida Francisco Salazar, Casilla 54-D, Temuco 01145, Chile
E-mail addresses: edward.hermosilla@uautonoma.cl (E. Hermosilla), olga.rubilar@ufrontera.cl (O. Rubilar).

https://doi.org/10.1016/j.eti.2026.105120
Received 9 June 2026; Received in revised form 15 July 2026; Accepted 18 July 2026
Available online 22 July 2026

> 97% activity over five cycles. These membranes are directly applicable as reusable, metal-free modules for textile-effluent decolorization under solar/visible illumination.

1. Introduction

The textile industry is among the largest industrial consumers of water and one of the most significant sources of colored effluent worldwide; a substantial fraction of the dyes applied during dyeing is lost to wastewater because of incomplete fixation to the fiber (Deogaonkar-Baride et al., 2025). Even at trace concentrations (<1 mg L^{-1}), colored discharges reduce light penetration and dissolved-oxygen exchange in receiving waters, impairing aquatic photosynthesis, while many synthetic dyes and their breakdown products are mutagenic, carcinogenic and highly recalcitrant (Islam et al., 2023). Conventional treatment trains (coagulation–-flocculation, adsorption, and biological processes) are limited for these effluents: they frequently transfer the pollutant to a secondary phase (sludge, spent adsorbent) rather than mineralizing it, and the aromatic, electron-deficient structure of dyes such as methylene blue resists conventional biodegradation (Raj et al., 2023). These limitations motivate advanced oxidation processes (AOPs) capable of on-site mineralization, and, in particular, solar-/visible-light-driven photocatalysis as a low-energy, chemical-lean route for textile-effluent remediation.

Beyond their environmental relevance, methylene blue (MB) and similar cationic thiazines serve as widely accepted probe molecules for benchmarking the performance of AOPs (Boulkhessaim et al., 2022; Buzga et al., 2022; Guo et al., 2021; Zhang et al., 2019; Zhu et al., 2023). Although these AOPs offer a pathway for mineralizing such pollutants, traditional metal-oxide photocatalysts (e.g., TiO_2, ZnO) impose significant practical limitations. Their wide band gaps restrict photoactivation to the UV range, which represents less than 5% of the solar spectrum, and their use introduces additional environmental concerns associated with heavy metal leaching (Ahmadian et al., 2023; Ennasraoui et al., 2026; Hassaan et al., 2023). Consequently, graphitic carbon nitride (g-C_3N_4) has emerged as a metal-free alternative. Structurally composed of tri-s-triazine units, g-C_3N_4 possesses an ideal visible-light-responsive band gap (~2.73 eV) and a highly negative conduction band potential that thermodynamically favors the reductive activation of dissolved oxygen into superoxide radicals, making it ideal for solar-driven remediation (Jiang et al., 2018; Wang et al., 2024). Despite its promise, the practical deployment of powdered g-C_3N_4 is severely hindered by the well-known "slurry problem": it tends to agglomerate in aqueous media, reducing the active surface area, and it is difficult to recover post-treatment, leading to secondary pollution and hindering continuous operation (Kalaitzidou and Merachtsaki, 2023; Pellegrino et al., 2017). Owing to its metal-free nature and visible-light response, g-C_3N_4 has been extensively coupled with second phases to suppress the fast recombination of photogenerated carriers. Mishra et al. constructed a Z-scheme g-C_3N_4/Gd_2O_3 heterojunction that narrowed the band gap to 2.58 eV and degraded 97% of ciprofloxacin and 96.5% of tetracycline within 120 min under visible light, with •OH and $•O_2^-$ identified as the driving species (Mishra et al., 2026b). A type-II g-C_3N_4/Sm_2O_3 system extended the absorption edge up to 550 nm and achieved ≥ 90% removal of ciprofloxacin, bisphenol A and Cr(VI) in 120 min, with $•O_2^-$ and h^+ as the main reactive moieties (Mishra et al., 2026a). Beyond pollutant abatement, S-scheme g-C_3N_4/α-MnO_2 nanojunctions have been shown to photoreform polystyrene into value-added chemicals and H_2 while mineralizing Reactive Blue 19 within minutes, again through an $•O_2^-$/•OH-mediated route (Mohanty et al., 2025). These works consistently show that the intrinsic activity of g-C_3N_4 is not the bottleneck, and that the reported strategies focus on band engineering rather than on the physical format of the catalyst. In parallel, cellulose and its derivatives have emerged as sustainable supports for water remediation, both as adsorbents and as photocatalyst carriers, owing to their abundance, biodegradability and dense surface hydroxyl chemistry, which provides anchoring sites and promotes interfacial charge transfer (Behera et al., 2025; Mishra et al., 2024). Cellulose extracted from waste bamboo culm sheath removed 92.8% of malachite green with a Langmuir capacity of 111.11 mg g^{-1} and > 80% retention after four cycles, confirming the intrinsic affinity of the biopolymer for cationic dyes (Behera et al., 2025). More relevant to the present work, Mishra et al. reported a g-C_3N_4/cellulose composite derived from modified banana leaves that degraded 93.4% of rhodamine B and 92.1% of methylene blue (30 mg L^{-1}) in 120 min under visible light, with $•O_2^-$ and h^+ as the dominant reactive oxygen species and 81% efficiency retained after five cycles; the cellulose fraction was shown to

Table 1
Comparative photocatalytic performance of CA membranes incorporating different photocatalysts for MB degradation.

Membrane / Photocatalyst	MB degradation (conditions)	Reuse performance	Identified reactive species	Fabrication method	Ref.
CA–Chitosan/BiOCl	79.9% in 60 min (UV)	3 cycles (78%)	O_2^-•, •OH	Casting	(Sasikala et al., 2024)
CA/TiO_2	64% in 120 min (UV)	Not tested	•OH, O_2^-•	Phase inversion	(Aljawrneh et al., 2022)
CA/ZnO	> 30% in 200 min (UV)	Not tested	O_2^-•, •OH	Phase inversion	(Asiri et al., 2022)
CA/ZnO nanoparticles	~75% in 120 min (sunlight)	5 cycles (72%)	O_2^-•, •OH	Phase inversion	(Abu-Dalo et al., 2021)
CA/Ag–CdSe/GO	~90% in 40 min (visible)	5 cycles (80.3%)	•OH, O_2^-•	Electrospinning	(El-Barbary et al., 2021)
CA/TiO_2 (P25)	99.1% in 30 min (UV)	5 cycles (97.5%)	O_2^-•, •OH	Electrospinning–electrospray	(Wang et al., 2024)
CA/PMMA@PDA@ZIF−67 (ZPP)	99.9% in 15 min (UV)	5 cycles (90.2%)	$^1O_2$, SO_4^-•, •OH, O_2^-•	Electrospinning–electrospray	(Tian et al., 2025)

disperse the g-C_3N_4, to increase the specific surface area from 14.0 to 37.9 $m^2\ g^{-1}$ and to mediate electron transfer through hydrogen bonding with the amino groups of the nitride (Mishra et al., 2025). As summarized in Table 1, most highly efficient MB photocatalysts are still deployed as non-recoverable powders, whereas the reported supported membranes either operate under UV or reach modest removals; a metal-free, visible-light-driven and readily recoverable membrane combining both attributes is still lacking.

In this sense, electrospun nanofibrous membranes provide an optimal architecture for this purpose, offering high specific surface area, interconnected porosity, and superior mass transfer channels that facilitate pollutant–catalyst interactions (Sabzehmeidani et al., 2021; Zheng et al., 2024). The selection of the supporting matrix is pivotal for designing sustainable catalytic platforms. Cellulose acetate (CA), a renewable and biodegradable derivative of cellulose, offers distinct advantages over petroleum-derived synthetic polymers (such as polyacrylonitrile or polyvinylidene fluoride), including excellent hydrophilicity, mechanical robustness, and chemical tunability (Manea et al., 2016). By integrating g-C_3N_4 into CA nanofibers, it is possible to engineer a "green" hybrid system that combines the intrinsic photocatalytic activity of the semiconductor with the processability and filtration capabilities of the biopolymer (Fatiatun et al., 2025; Islam et al., 2023). The major objective of combining both components is therefore functional complementarity rather than a simple additive effect: g-C_3N_4 supplies the visible-light photoactivity that the biopolymer lacks, whereas CA supplies dispersion, macroscopic handling, recovery, hydrophilicity and an accessible porous architecture that the powder lacks.

Herein, we report the fabrication of CA/g-C_3N_4 nanocomposite membranes via electrospinning as a technological solution for continuous, sustainable wastewater treatment. Unlike previous studies that struggle with particle dispersibility or rely on simple physical mixtures, we optimized the spinning parameters to achieve a uniform distribution and an interfacial electronic coupling of g-C_3N_4 nanosheets within the CA matrix. We systematically evaluated the physicochemical properties, visible-light photocatalytic performance, and reactive species mechanisms of the composite using MB as a model target. The resulting membranes demonstrate not only superior degradation efficiency compared to conventional phase-inversion counterparts but also good reusability. This work establishes a scalable, metal-free, and bio-derived platform for the efficient decontamination of textile effluents, effectively overcoming the technological barriers of powder-based photocatalysis.

2. Materials and methods

2.1. Synthesis of g-C_3N_4

Graphitic carbon nitride (g-C_3N_4) was synthesized via thermal polymerization following a modified procedure described by Pincheira et al. (2025). Briefly, 10 g of urea (CAS 57–13–6) was placed in a ceramic crucible and heated at 550 °C for 2 h in a muffle furnace (Thermolyne 1400, Thermo Fisher Scientific, USA). The resulting pale-yellow product was ground in an agate mortar into a fine powder and stored in airtight glass vials under ambient conditions.

2.2. Characterization of g-C_3N_4

The hydrodynamic particle size and zeta potential were determined using dynamic light scattering (DLS; Zetasizer Nano ZS90, Malvern Instruments, UK). Optical properties were analyzed via UV–vis spectroscopy (Thermo Scientific Evolution™ 60S), while morphological and structural features were examined using transmission electron microscopy (TEM; JEOL 1200 EX II, Japan). Crystalline phase identification was performed by X-ray diffraction (XRD) using a Bruker D8 Advance diffractometer (Germany).

2.3. Photocatalytic activity of dispersions

Photocatalytic performance was evaluated using aqueous methylene blue (MB; CAS 61–73–4) solutions (10 mg L^{-1}). Experiments were conducted in a custom-built cylindrical photoreactor (15 cm inner diameter) internally lined with 5 m of white LED strips (120 LEDs m^{-1}). The average irradiance at the sample position was approximately 20 mW cm^{-2}, measured using a calibrated Thorlabs PM100D optical power meter equipped with an S425C thermal sensor (Ø27 mm active detector area). The sensor was positioned at the geometric center of the empty reactor, corresponding to the location occupied by the sample during the photocatalytic experiments. Four independent measurements were acquired, rotating the sensor by 90° between successive readings to verify the azimuthal symmetry of the illumination, and the reported irradiance corresponds to their average. During the experiments, the reaction suspension (50 mL) was magnetically stirred at 200 rpm to minimize local concentration gradients. Prior to irradiation, adsorption–desorption equilibrium was established by stirring in the dark for 30 min. During visible-light irradiation (4 h), 1 mL aliquots were withdrawn every 30 min, centrifuged (13,000 rpm, 5 min), and analyzed by UV–vis spectroscopy ($\lambda_{max} = 665$ nm). Degradation efficiency was expressed as C/C_o, and kinetics were analyzed using the pseudo-first-order model $\ln(C_o/C) = kt$.

2.4. Reactive species scavenging

To elucidate the degradation mechanism, radical scavenging assays were performed under optimized conditions (0.6 g L^{-1} g-C_3N_4, pH 10). Scavengers were introduced at a final concentration of 1 mM: hydroquinone for superoxide radicals ($\bullet O_2^-$), *tert*-butyl alcohol for hydroxyl radicals (•OH), sodium azide for singlet oxygen ($^1O_2$), EDTA for holes (h^+), and silver nitrate for electrons (e^-). The experimental protocol followed that of Section 2.3, with residual MB concentrations determined after 240 min of irradiation.

2.5. Fabrication of electrospun membranes

Cellulose acetate (CA; CAS 9004–35–7) solutions were prepared at concentrations of 5, 10, and 15% (w/v) in acetone (CAS 67–64–1), dimethyl sulfoxide (DMSO; CAS 67–68–5), or binary mixtures (1:1 or 2:1 v/v). Homogeneity was ensured by magnetic stirring (500 rpm, 24 h). Electrospinning was conducted using a NEU-BM unit (Tongli Technology, China) with a feed rate of 2 mL h^{-1}, a tip-to-collector distance of 13 cm, and an applied voltage of 20 kV. Nanofibers were collected on an aluminum foil-covered rotating drum (50 rpm).

2.6. Fabrication of CA/g-C_3N_4 membranes

Composite membranes were fabricated by dissolving 15 wt% CA in an acetone:DMSO (2:1 v/v) solvent system containing dispersed g-C_3N_4 at loadings of 0.5, 1.0, and 2.0 wt%. The mixtures were stirred (500 rpm, 24 h) to ensure uniform dispersion prior to electrospinning under the parameters described in Section 2.5. The resulting membranes are designated as CA/g-C_3N_4−0.5, CA/g-C_3N_4−1, and CA/g-C_3N_4−2. The overall fabrication route of the CA/g-C_3N_4 composite membranes, from g-C_3N_4 synthesis to the electrospun nanofibrous membrane, is summarized in Scheme 1.

2.7. Membrane characterization

Membrane morphology was analyzed by scanning electron microscopy (SEM; Hitachi SU3500, Japan). Average fiber diameters were calculated from SEM micrographs using ImageJ software ($n \geq 100$ fibers), and membrane thickness was measured using a digital micrometer. Chemical structure and surface functional groups were characterized by Fourier transform infrared spectroscopy (FTIR) using a Cary−630 spectrometer (Agilent Technologies Inc., Santa Clara, CA) equipped with an attenuated total reflectance (ATR) accessory. Spectra were acquired in the range of 4000–600 cm^{-1} with a resolution of 4 cm^{-1} and 32 scans per sample. Textural properties, including specific surface area (SSA) and pore size distribution, were determined using a Quantachrome Nova 1200e surface analyzer. Prior to analysis, samples (0.10–0.15 g) were degassed at 110 °C for 24 h under a continuous flow of nitrogen gas. N_2 adsorption–desorption isotherms were recorded at 77 K, and the specific surface area was calculated using the Brunauer–Emmett–Teller (BET) model (Prabu et al., 2022).

2.8. Photocatalytic performance of membranes

Rectangular specimens of 3.6 × 5.0 cm were mounted on a custom 3D-printed polylactic acid (PLA) holder facing the light source. The membranes were immersed in 100 mL of MB solution (10 mg L^{-1}). Given the radial illumination of the photoreactor, both sides of the membrane were irradiated simultaneously, yielding a total effective exposed area of approximately 36 cm^2 (discounting the minimal surface shielded by the holder). Degradation assays were carried out in the LED photoreactor (Section 2.3) with continuous stirring (200 rpm). Aliquots were sampled at 30 min intervals and analyzed spectrophotometrically.

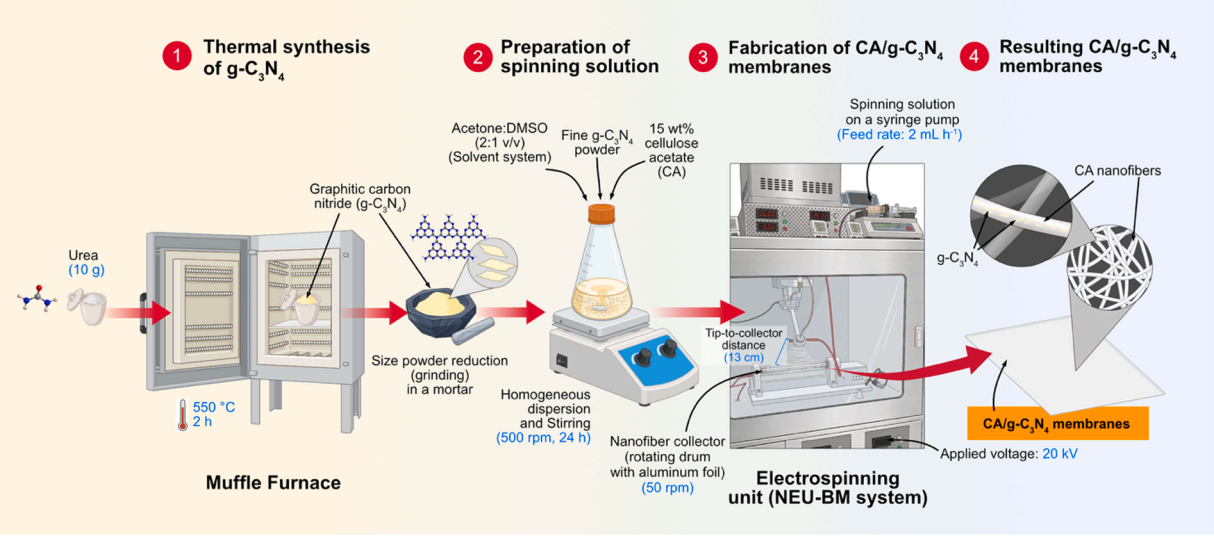

Scheme 1. Fabrication route of the CA/g-C_3N_4 membranes.

2.9. Recovery and reusability

For regeneration, spent membranes were removed from the dye solution, gently blotted and exposed to the same LED source in air (dry state) for 1 h at room temperature (~25 °C) and ambient relative humidity, without any solvent or thermal treatment. The reusability and operational stability of the membranes were subsequently evaluated over five consecutive photocatalytic cycles under identical testing conditions.Fig. 1

3. Results and discussion

3.1. Synthesis and characterization of g-C_3N_4

The optical and structural properties of the synthesized g-C_3N_4 were elucidated via UV–vis spectroscopy, TEM, and XRD. The UV–vis spectrum (Fig. 2a) displays a broad absorption profile typical of semiconductor materials, characterized by a strong band between 250–400 nm and a tail extending into the visible region (~700 nm). The absorption edge at ~403 nm corresponds to an optical band gap of 2.73 eV (Fig. 2b), a value consistent with reported ranges (2.7–2.8 eV) for polymeric g-C_3N_4 and confirming its suitability for visible-light-driven photocatalysis (Jiang et al., 2018; Madankar et al., 2025; Swetha et al., 2025).

Morphologically, TEM analysis (Fig. 2c) reveals a stacked, nanosheet architecture. Unlike bulk g-C_3N_4, which typically forms dense, block-like aggregates, this layered morphology offers a higher specific surface area and significantly shorter diffusion distances for photogenerated charge carriers. This morphological advantage inherently mitigates the rapid electron-hole recombination often associated with bulk g-C_3N_4, facilitating superior pollutant adsorption and exciton utilization prior to its immobilization in the polymer matrix.

The structural integrity was further corroborated by XRD (Fig. 2d), which shows two distinct diffraction peaks: a weak reflection at 13.8° indexed to the (100) plane (in-plane repeating tri-s-triazine units) and a strong reflection at 27.3° indexed to the (002) plane (interlayer stacking of aromatic systems) (Alizadeh et al., 2019). The sharpness of these peaks indicates a high degree of crystallinity and well-preserved polymeric ordering.

3.2. Photocatalytic degradation of MB by g-C_3N_4 under dispersion conditions

To establish a baseline for catalytic performance and highlight the inherent limitations of powder suspensions, MB degradation was evaluated using g-C_3N_4 dispersions (0.4 and 0.6 g L^{-1}) under visible-light irradiation (λ>400 nm). The LED source spectrum (Fig. 1b) confirms a strong emission band between 400–480 nm with a broad tail from 500 to 700 nm and the absence of UV emission, ensuring that degradation is driven exclusively by visible-light excitation. The photocatalytic efficiency of the suspended powder exhibited a strong pH dependence (Fig. 3). While performance was modest at pH 5, alkaline conditions significantly enhanced activity. At pH 10, adsorption in the dark reached ~27% (compared to negligible adsorption at pH 5), and total degradation reached 90.9% after 240 min ($k_{app} = 0.83 \times 10^{-2}$ min^{-1}). While highly alkaline conditions are not universally favorable for all advanced oxidation processes, they are highly synergistic for this specific system. This pH-dependent enhancement is driven by electrostatic interactions: as the pH rises above the pKa of MB (3.8), the dye remains cationic, while the g-C_3N_4 surface becomes increasingly negative (zeta potential: –45.2 mV at pH 10, Table 2). This strong electrostatic attraction brings the pollutant into proximity with surface active sites, facilitating charge transfer. Furthermore, alkaline environments specifically promote the generation and stabilization of superoxide radicals ($O_2^{\bullet-}$), the dominant oxidative species for this reductive pathway (Vera et al., 2025).

Notably, the reaction rate of pristine g-C_3N_4 (0.83×10^{-2} min^{-1}) is comparable to reported binary composites such as TiO_2/g-C_3N_4 (0.4×10^{-2} min^{-1}) or ZnO/g-C_3N_4 (0.21×10^{-3} min^{-1}) (Ashwini et al., 2025; Shakoor et al., 2024; Zhuang et al., 2019), highlighting

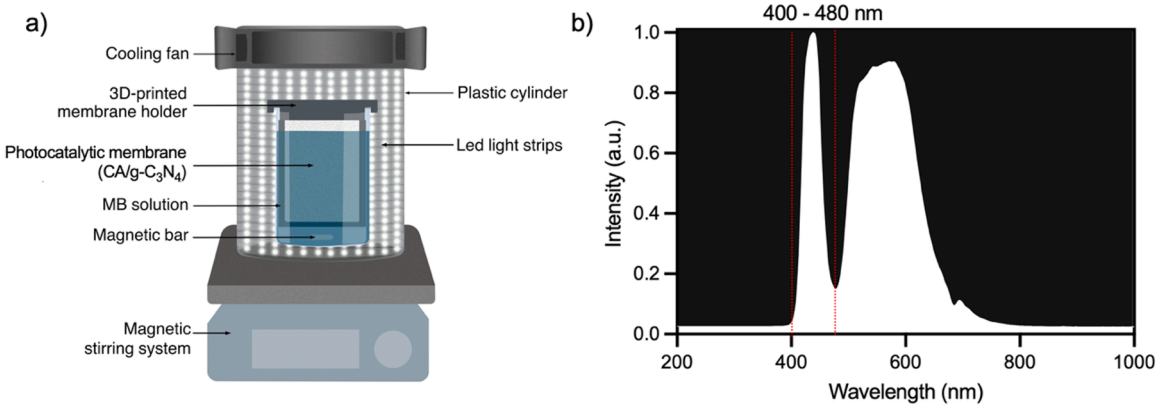

Fig. 1. Schematic representation of the photocatalytic reactor setup (a) and emission spectrum of the LED array employed as the irradiation source (b).

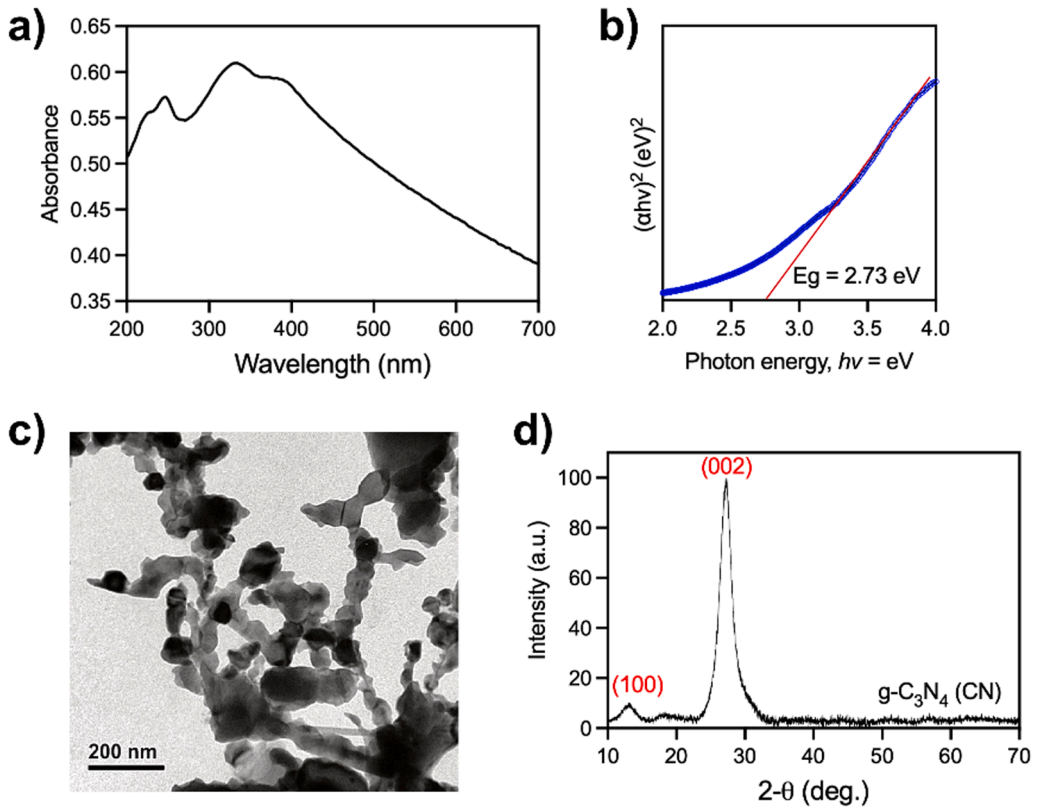

Fig. 2. Structural and optical characterization of synthesized g-C_3N_4: (a) UV–vis absorption spectrum, (b) Tauc plot for bandgap estimation, (c) TEM image, and (d) XRD pattern.

the intrinsic potential of this metal-free catalyst without the environmental risks associated with heavy metal leaching. However, this strict requirement for an optimal pH of 10 and the inherent difficulties in recovering the suspended powder post-treatment severely limit its practical utility. This underscores the technological requirement of engineering a supported membrane system that not only prevents secondary pollution but also operates effectively across a broader pH window.

3.3. Mechanism of reactive species generation

To identify the reactive species involved in the degradation mechanism, scavenger assays were conducted under optimal photocatalytic conditions (Fig. 4). The introduction of hydroquinone ($\bullet O_2^-$ scavenger) inhibited degradation by 72.2%, which, together with the electron-scavenging results, indicates superoxide radicals as the predominant oxidative species. Sodium azide ($^1O_2$ quencher) reduced efficiency by 44.2%, indicating a significant secondary role for singlet oxygen. Similarly, silver nitrate, acting as an electron scavenger, suppressed degradation by 66.6%, highlighting the central role of conduction-band (CB) electrons in driving oxygen activation. Conversely, scavengers for hydroxyl radicals (•OH) and photogenerated holes (h^+) showed minimal inhibition (22.9% and 9.4%, respectively).

These findings demonstrate that MB degradation over g-C_3N_4 proceeds predominantly via a reductive oxygen-activation mechanism, initiated by CB electrons reducing dissolved oxygen into $\bullet O_2^-$. The partial suppression by sodium azide further supports the formation of $^1O_2$, either through direct energy transfer from photoexcited g-C_3N_4 to O_2, or via sequential transformations involving $\bullet O_2^-/H_2O_2$. In contrast, the weak inhibition observed for •OH and h^+ scavengers is consistent with the intrinsic band structure of g-C_3N_4: under visible-light excitation (≈450 nm, ~2.73 eV), the CB potential (−1.1 to −1.3 V vs. NHE) is sufficiently negative to activate O_2 into $\bullet O_2^-$, whereas the VB potential (+1.4 to +1.6 V vs. NHE) is insufficient to oxidize water ($E^\circ(H_2O/\bullet OH) = +2.38$ V vs. NHE), thus limiting hydroxyl radical generation (Molaei, 2023; Niu et al., 2021). This reductive interpretation is independently corroborated by recent g-C_3N_4/calcite-based studies. By combining scavenger assays, Mott–Schottky analysis, and EPR, these reports similarly confirmed that the semiconductor's band alignment structurally suppresses hole-driven oxidation in favor of an electron-driven pathway (Zhang et al., 2024, 2025).

The proposed sequence is therefore:

$$\text{g-}C_3N_4 + h\nu\ (\lambda > 400\ \text{nm}) \rightarrow e^-(CB) + h^+(VB) \quad (1)$$

$$e^-(CB) + O_2 \rightarrow \bullet O_2^- \quad (2)$$

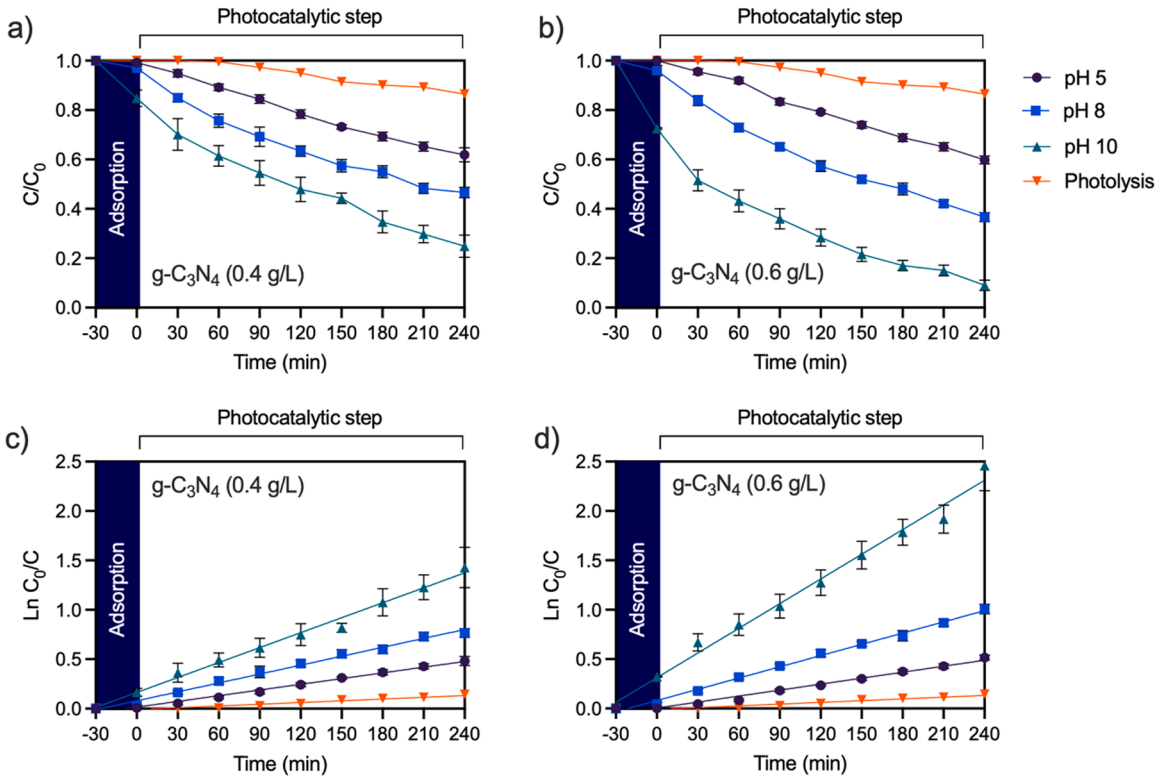

Fig. 3. Photocatalytic degradation of methylene blue (MB) by dispersed g-C_3N_4 under different pH conditions and catalyst loadings: (a–b) 0.4 g·L^{-1} and (c–d) 0.6 g·L^{-1} . The dark adsorption equilibrium phase (−30–0 min) precedes visible-light irradiation.

Table 2
Apparent rate constants (k_{app}), MB degradation efficiencies, and zeta potentials of g-C_3N_4 dispersions at different pH values and catalyst loadings.

pH	Catalyst loading (g L^{-1})				Zeta potential (mV)
	0.4		0.6		
	k_{app} (10^{-2} min^{-1})	Efficiency (%)	k_{app} (10^{-2} min^{-1})	Efficiency (%)	
5	0.192	38.1 ± 4.9c	0.202	40.1 ± 2.7c	22.4 ± 0.7
8	0.301	53.4 ± 3.6b	0.379	63.3 ± 3.1b	−11.4 ± 1.3
10	0.504	75.0 ± 0.9a	0.833	90.9 ± 3.6a	−45.2 ± 1.6

Different letters indicate significant differences ($p < 0.05$).

$$\bullet O_2^- + h^+ \rightarrow {}^1O_2 \text{ (or g-}C_3N_4{}^* + O_2 \rightarrow {}^1O_2) \quad (3)$$

$$\text{MB(ads)} + \bullet O_2^-/{}^1O_2 \rightarrow \text{demethylated/ring-opened intermediates} \quad (4)$$

Reaction (1) generates the charge carriers; the electrons reduce O_2 to $\bullet O_2^-$ (2), the main oxidant, while a fraction is converted to $^1O_2$ (3), accounting for the partial inhibition by sodium azide. Both species attack MB previously adsorbed on the catalyst surface (4). Because $\bullet O_2^-$ and $^1O_2$ are short-lived, degradation occurs essentially at the surface, and adsorption is a prerequisite rather than a competing process. This also rationalizes the pH dependence described in Section 3.2: alkaline media stabilize $\bullet O_2^-$ and simultaneously promote the accumulation of cationic MB on the negatively charged catalyst, which is why both the extent of dark adsorption and k_{app} increase with pH.

At the molecular level, the identified species act on the electron-rich sites of the MB chromophore. As a cationic thiazine dye, MB is reported to degrade in $\bullet O_2^-/{}^1O_2$-driven systems through successive N-demethylation of its auxochromic dimethylamino groups, yielding azure B, azure A, azure C and thionine, followed by cleavage of the central C–S^+=C chromophore, ring opening of the resulting aromatic fragments and subsequent oxidation to low-molecular-weight carboxylic acids and inorganic ions (SO_4^{2-}, NO_3^-, NH_4^+) (González and Jaramillo-Fierro, 2025; Zhang et al., 2002). The progressive decay of the 665 nm absorption band observed here is consistent with the destruction of this chromophore. We note, however, that MB removal in this study was quantified spectrophotometrically at λ_{max} = 665 nm, which reports chromophore destruction (decolorization) rather than complete mineralization.

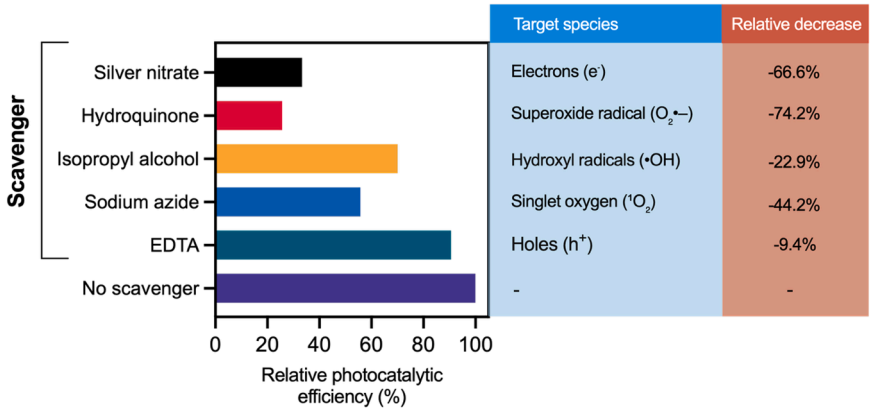

Fig. 4. Effect of reactive species scavengers on the photocatalytic degradation of MB by g-C_3N_4. Assay conditions: 0.6 g L^{-1} of g-C_3N_4, pH 10, 240 min of visible-light irradiation.

Identification of the transformation intermediates by LC–MS/MS and quantification of the mineralization degree by total organic carbon (TOC) analysis were beyond the analytical scope of this work and are identified as priorities for future study.

This mechanistic pathway is consistent with several recent reports, where g-C_3N_4-based photocatalysts demonstrated dominant $\bullet O_2^-$ generation, with •OH radicals playing only a minor role. For instance, Phakathi et al. (2025) observed a similar suppression pattern in dye degradation, while Solayman et al. (2024) and Wang et al. (2024) reported that oxygen-centered radicals govern most g-C_3N_4-driven photocatalytic processes. Yang et al. (2021) further highlighted that the low VB potential of g-C_3N_4 inherently favors reductive over oxidative pathways. The scavenger assays underscore the electron-driven reductive oxygen activation mechanism of pristine g-C_3N_4, with $\bullet O_2^-$ as the principal species and $^1O_2$ as an auxiliary oxidant. We acknowledge that radical-scavenging assays provide indirect evidence of the reactive species involved; direct spectroscopic confirmation by EPR spin-trapping with DMPO, as applied to analogous g-C_3N_4-based photocatalysts (Zhang et al., 2025), is recommended as the natural next step to unambiguously verify the $\bullet O_2^-$ and $^1O_2$ pathways.

3.4. *Preparation and characterization of CA/g-C_3N_4 electrospun membranes*

Achieving a stable, reusable membrane requires balancing polymer processability with catalyst accessibility. Prior to composite membrane fabrication, the electrospinning conditions for pure CA membranes were systematically assessed to ensure a robust structural template. CA concentrations (10 and 15 wt%) and solvent systems comprising acetone, dimethyl sulfoxide (DMSO), and their binary mixtures (acetone:DMSO ratios of 1:1 and 2:1, v/v) were evaluated (Table 3). It was observed that when acetone or DMSO was employed as a single solvent, no fibrous membrane formation occurred, highlighting the necessity of mixed solvent systems to balance volatility and conductivity during jet formation (Attari and Hausler, 2020; Neukirch et al., 2024). The optimization revealed that a 15% CA solution in a 2:1 binary solvent system produced uniform, continuous nanofibers with a robust membrane architecture. The successful fiber formation is attributed to the optimized viscosity and solvent volatility at this formulation, which ensured sufficient polymer chain entanglement and stable stretching of the electrospun jet.

Based on these optimized parameters, composite membranes were fabricated by introducing g-C_3N_4 at loadings of 0.5, 1.0, and 2.0 wt%. SEM analysis revealed that composite membranes preserved uniform morphology (Fig. 5a and Fig. 5e), while EDS mapping

Table 3
Effect of solvent composition and cellulose acetate (CA) concentration on membrane formation during electrospinning.

Solvent	CA concentration (%)	Electrospun membrane formation (+/–)
Acetone	10	-
	15	-
DMSO	10	-
	15	-
Acetone:DMSO 1:1	10	-
	15	-
Acetone:DMSO 2:1	10	-
	15	+

All membranes were synthesized at an applied voltage of 20 kV.
"+" indicates successful electrospun membrane was obtained.
"–" indicates that no electrospun membrane was obtained; instead, the process resulted in electrosprayed particles or non-homogeneous CA deposition.

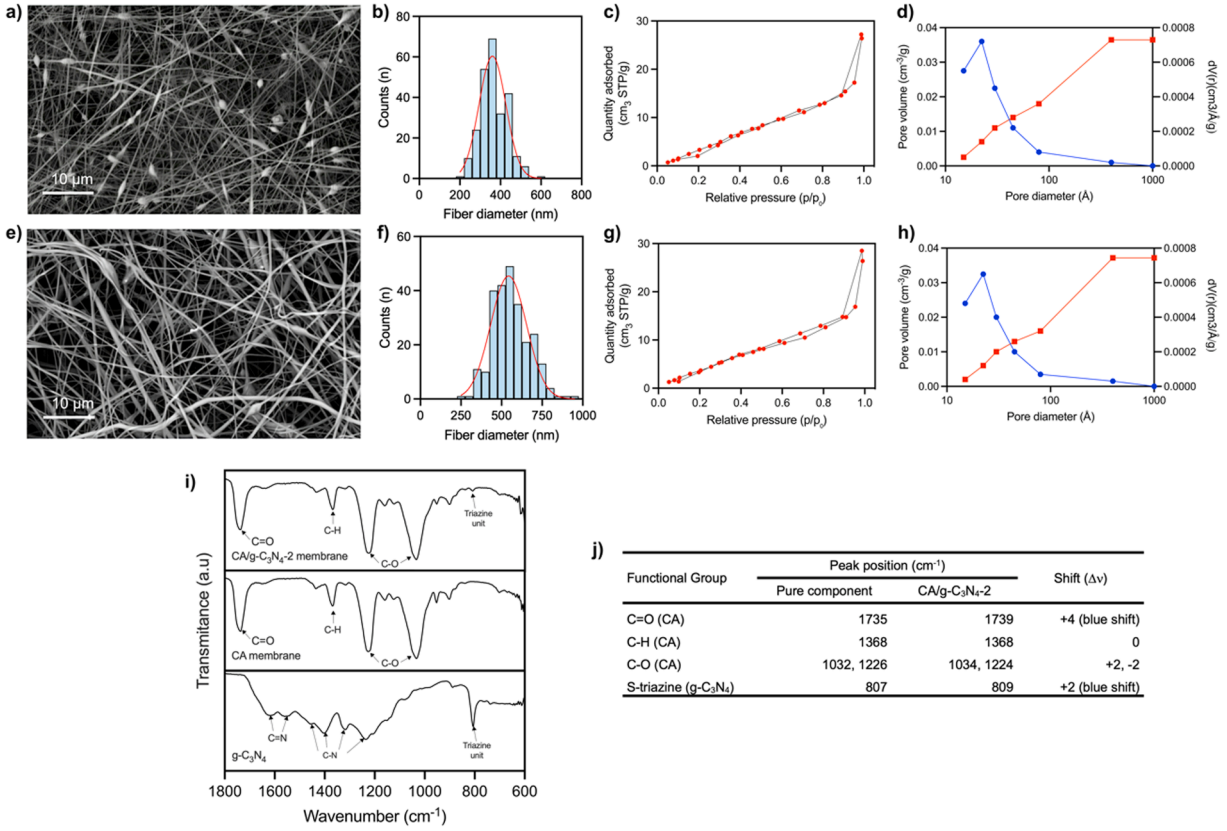

j)

Functional Group	Peak position (cm^{-1})		Shift (Δν)
	Pure component	CA/g-C_3N_4-2	
C=O (CA)	1735	1739	+4 (blue shift)
C-H (CA)	1368	1368	0
C-O (CA)	1032, 1226	1034, 1224	+2, -2
S-triazine (g-C_3N_4)	807	809	+2 (blue shift)

Fig. 5. Characterization of pure CA (a–d) and CA/g-C_3N_4−2 membranes (e–h). SEM micrographs, fiber diameter distributions, and porosity analysis (N_2 isotherms and BJH pore size) for both samples. (i, j) FTIR spectra and peak shift table comparing chemical interactions.

demonstrated a homogeneous distribution of nitrogen across the surface, confirming the successful and uniform dispersion of g-C_3N_4 within the membrane matrix (Figure S1). Interestingly, X-ray photoelectron spectroscopy (XPS) analysis of the composite membrane surface did not reveal significant nitrogen signals (Figure S2). Considering the surface-sensitive nature of XPS (probing only the top 5–10 nm) compared to the deeper penetration volume of EDS (~1–3 µm), this discrepancy provides critical insight into the membrane architecture. It indicates that the nanosheets are not merely deposited on the fiber exterior but are intimately encapsulated within a thin layer of the CA polymer matrix. This encapsulation, driven by solvent evaporation dynamics during electrospinning, is a highly desirable technological feature: it physically anchors the photocatalyst, preventing leaching and ensuring the long-term operational stability and reusability of the membrane without causing secondary pollution.

At higher magnification, the composite nanofibers exhibited increased thickness (average diameter 556.2 nm) compared to pure CA fibers. This increase in diameter confirms the effective integration of the photocatalyst within the fibrous network without compromising its structural integrity. To verify the chemical nature of the integration and address the potential for interfacial interactions, FTIR analysis was performed (Fig. 5i and j). Crucially, among the observed spectral shifts, a blue shift (+4 cm^{-1}) of the C═O stretching band (1735 → 1739 cm^{-1}) suggests a disruption of CA self-association, where the filler physically hinders the formation of inter-chain CA-CA hydrogen bonds. Simultaneously, the blue shift (+2 cm^{-1}) of the s-triazine breathing mode (807 → 809 cm^{-1}) evidences structural rigidification and an electronic perturbation of the g-C_3N_4 lattice. This electronic perturbation, induced by the forced integration during the high-voltage electrospinning process, is a key technological feature that indicates an intimate interfacial coupling rather than simple physical entrapment. Although a direct quantification of charge-carrier dynamics is beyond the scope of the present characterization, such interfacial coupling is commonly associated with facilitated charge separation and would be consistent with the enhanced photocatalytic efficiency observed for the composite membranes. We note that the inference of improved interfacial charge separation is based on vibrational (FTIR) evidence; direct photoelectrochemical validation by photoluminescence, transient photocurrent and electrochemical impedance spectroscopy is identified as a priority for future work.

The decrease in specific surface area upon g-C_3N_4 loading (28.6–20.2 m^2 g^{-1}) can be assigned to a specific mechanism by cross-analyzing the fiber-morphology and porosimetry data (Fig. 5c, d, g, and h). Two possibilities, pore blockage and partial structural collapse, can be ruled out: the cumulative pore volume and the average (BJH) pore diameter remained invariant between pristine CA and CA/g-C_3N_4−2, indicating that the internal mesopore network (which originates from solvent-evaporation channels within the CA matrix) is preserved intact. Instead, the reduction is governed by two geometric/gravimetric factors. First, SEM analysis shows a marked increase in mean fiber diameter after loading (from 360.3 nm to 556 nm); because the external surface-area-to-volume ratio of

a cylindrical fiber scales inversely with its diameter, thicker fibers inherently expose less geometric surface per unit mass. Second, the embedded g-C_3N_4, a comparatively dense, low-porosity filler, adds mass without contributing proportional surface area, thereby diluting the gravimetric (per-gram) surface area of the composite. In short, the SSA reduction reflects fiber thickening and mass dilution by the filler, not destruction or obstruction of the porous architecture, consistent with the retention of pore volume, pore size and, ultimately, of efficient mass-transfer channels for pollutant–catalyst contact. From a sustainability perspective, it is worth noting that while other reported g-C_3N_4 membranes rely on petroleum-derived polymers like PAN or PVDF, the use of CA, a renewable and biodegradable biopolymer, underscores the eco-friendly innovation of this supported photocatalyst (Borban et al., 2023; Song et al., 2023). This technological choice aligns the system with green chemistry principles while solving the practical recovery issues of powder-based systems.

3.5. Photocatalytic degradation of MB by CA/g-C_3N_4 membranes

The immobilized CA/g-C_3N_4 membranes demonstrated robust photocatalytic activity, effectively overcoming the mass-transfer and light-harvesting limitations of conventional solid supports. Performance was positively correlated with both catalyst loading (0.5–2 wt%) and pH. Kinetic profiles were followed every 30 min over 240 min after 30 min of dark equilibration (Fig. 6a–d). Degradation follows pseudo-first-order kinetics ($\ln(C_o/C) = k \cdot t$, $R^2 > 0.98$; Fig. 6e–h). Removal is fastest during the first 60–90 min, when both the dye concentration and the density of free active sites are maximal, and progressively plateaus as MB is consumed; $>$ 90% removal is already reached at ~180 min at pH 10, with 98.7% at 240 min.

The results of MB degradation after 240 min of photocatalysis, together with apparent rate constants (k_{app}), are summarized in Table 4. At pH 5, MB removal ranged from 43.3% (CA/g-C_3N_4−0.5, $k_{app} = 0.224 \times 10^{-2}$ min^{-1}) to 83.0% (CA/g-C_3N_4−2, $k_{app} = 0.665 \times 10^{-2}$ min^{-1}). A pronounced enhancement was observed under neutral to alkaline conditions: at pH 8, efficiencies reached 63.3% (CA/g-C_3N_4−0.5), 82.0% (CA/g-C_3N_4−1), and 97.9% (CA/g-C_3N_4−2), with k_{app} values increasing accordingly. The highest activity was obtained at pH 10, where MB degradation achieved 85.7% (CA/g-C_3N_4−0.5, $k_{app} = 0.687 \times 10^{-2}$ min^{-1}), 96.5% (CA/g-C_3N_4−1, $k_{app} = 1.149 \times 10^{-2}$ min^{-1}), and 98.7% (CA/g-C_3N_4−2, $k_{app} = 1.668 \times 10^{-2}$ min^{-1}).

These results clearly demonstrate that both g-C_3N_4 loading and solution pH strongly influence photocatalytic performance. Higher photocatalyst loadings provided greater light absorption and more active sites, with the CA/g-C_3N_4−2 membrane consistently outperforming lower loadings. Nonetheless, the relatively small difference in efficiency between the CA/g-C_3N_4−1 and CA/g-C_3N_4−2 membranes at pH 10 (96.5% vs. 98.7%) suggests that performance approaches a saturation limit beyond which additional photocatalyst yields minimal benefit. Mechanistically, this plateau occurs because excessive photocatalyst loading within the finite fiber volume leads to particle stacking and increased opacity, which restricts light penetration and induces internal light scattering (shielding effects), thereby limiting the photoactivation of deeper catalytic sites.

The photocatalytic activity increased monotonically with pH. MB remains cationic above its pKa (3.8), while the embedded g-C_3N_4, the only pH-responsive component of an otherwise near-neutral cellulose acetate matrix, develops an increasingly negative surface charge under alkaline conditions. The resulting electrostatic attraction is evidenced functionally by the dark-adsorption data: MB uptake by CA/g-C_3N_4−2 at pH 10 exceeds that of pristine CA by 63% (Fig. 7), consistent with accumulation of the cationic dye on the catalyst-bearing surface. This pre-concentration brings the pollutant into the immediate vicinity of the active sites and facilitates interfacial charge transfer; in parallel, alkaline media favor the formation and stabilization of $\bullet O_2^-$, the dominant species here. Notably, the difference between pH 8 and pH 10 is not statistically significant ($p > 0.05$) for CA/g-C_3N_4−2, i.e. the membrane operates over a broad alkaline window, an operational advantage over the dispersion, which strictly requires pH 10. This insensitivity to slight pH

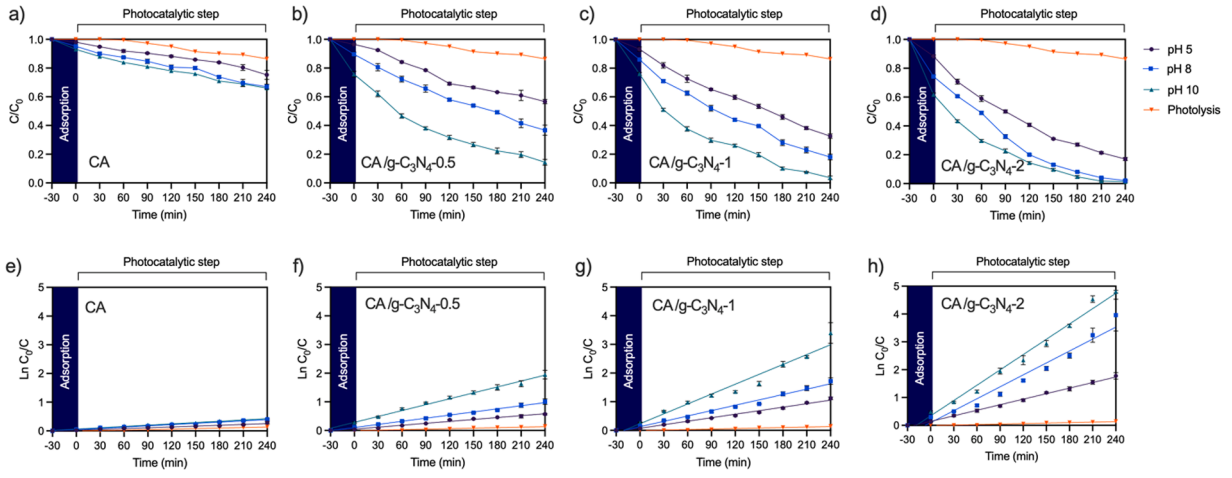

Fig. 6. Photocatalytic degradation kinetics of MB using CA and CA/g-C_3N_4 membranes under LED-light irradiation: (a–d) normalized concentration profiles (C/C_o) at pH 5, 8, and 10 following 30 min of dark adsorption and 240 min of irradiation; (e–h) corresponding kinetic plots. The influence of g-C_3N_4 loading (0.5, 1.0, and 2.0 wt%) is compared with pristine CA membranes.

Table 4
Apparent rate constants (k_{app}) and MB removal efficiencies of CA/g-C_3N_4 membranes at varying pH values and g-C_3N_4 loadings.

pH	Photocatalytic CA/g-C_3N_4 membrane					
	CA/g-C_3N_4−0.5		CA/g-C_3N_4−1		CA/g-C_3N_4−2	
	k_{app} (10^{-2} min^{-1})	Efficiency (%)	k_{app} (10^{-2} min^{-1})	Efficiency (%)	k_{app} (10^{-2} min^{-1})	Efficiency (%)
5	0.224	43.3 ± 1.53c	0.409	67.3 ± 1.52c	0.665	83.0 ± 2.00c
8	0.362	63.3 ± 3.5b	0.624	82.0 ± 2.00b	1.430	97.9 ± 1.00a
10	0.687	85.7 ± 2.1a	1.149	96.5 ± 1.32a	1.668	98.7 ± 1.53a

Different letters indicate significant differences ($p < 0.05$).

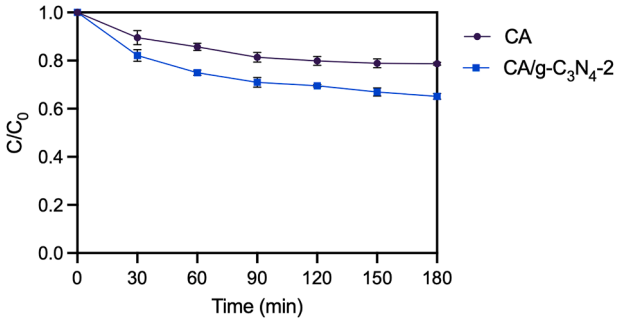

Fig. 7. Adsorption of MB under dark conditions by CA and CA/g-C_3N_4−2 membranes at pH 10.

fluctuations effectively eliminates the need for the strict, resource-intensive pH control systems typically required for variable textile effluents.

Critically, the electrospun architecture proved superior to conventional designs. Phase-inversion membranes reported in the literature often suffer from low porosity and poor catalyst exposure (e.g., reaching only ~30% degradation with ZnO (Asiri et al., 2022)). Other studies showed that phase-inversion CA membranes containing TiO_2, CeO_2, or TiO_2-CeO_2 reached only 64%, 7%, and 15% degradation, respectively, after 120 min (Aljawrneh et al., 2022). In contrast, our electrospun membranes offer a hierarchical, porous structure that maximizes light harvesting and mass transfer, allowing near-complete degradation under visible light. While these degradation assays in deionized water establish a highly robust proof-of-concept baseline for the material's architecture, practical deployment in large-scale remediation will necessitate further evaluation of these membranes against complex wastewater matrices, where competing ions and diverse organic constituents may influence surface reaction kinetics.

3.6. Synergistic adsorption and degradation

The dark-adsorption capacity of the biopolymer pre-concentrates the cationic dye at the catalytic sites, so that the two functions act synergistically rather than in parallel. Dark adsorption assays (Fig. 7) revealed that g-C_3N_4 incorporation increased dye uptake by 63% compared to pristine CA. Specifically, MB removal increased from 21.3% (CA) to 34.8% (CA/g-C_3N_4−2). This improvement is attributed to the introduction of g-C_3N_4, which contributes additional active sites, π-π interactions, and surface functionalities favorable for dye adsorption (Madankar et al., 2025).

Rather than acting as two isolated parallel processes, the adsorption contribution plays a critical synergistic role during photocatalytic degradation. Enhanced dye uptake at the membrane surface acts as a crucial pre-concentration step, increasing the local concentration of pollutants near the photocatalyst. By confining the MB molecules within the immediate vicinity of the g-C_3N_4 active sites, the system effectively overcomes the mass-transfer limitations typically observed in bulk solutions (Ahmadi et al., 2025; Salehi et al., 2024). This facilitates more efficient generation and transfer of reactive oxygen species upon light irradiation. To move beyond a qualitative description, the relative contributions of these pathways were deconvoluted via kinetic splitting using dark-adsorption and photolysis control data. For the CA/g-C_3N_4−2 membrane at pH 10, the overall 98.7% MB removal can be split into three distinct pathways: dark adsorption accounted for 34.8% of the removal (≈35.3% of the total contribution), direct photolysis of the dye under visible light contributed 13.6% (≈13.8% of the total), and true catalyst-driven photo-oxidation accounted for the remaining 50.3% (≈50.9% of the total). Crucially, the adsorption and photocatalytic pathways are not merely additive: the 63% enhancement of dark uptake conferred by g-C_3N_4 pre-concentrates the dye at the catalyst surface, significantly shortening the diffusion distance between the adsorbed MB and the short-lived reactive oxygen species, thereby accelerating the surface reaction upon irradiation. This use of a dark adsorption stage to pre-concentrate the target pollutant prior to visible-light degradation is consistent with recent g-C_3N_4-based systems that couple adsorption and photocatalysis to overcome mass-transfer limitations (Zhang et al., 2024).

Such combined adsorption-photocatalysis mechanisms have been widely reported as a key strategy to accelerate surface reaction kinetics and maximize overall pollutant degradation. The improvement observed in the present work is consistent with previous

studies where incorporation of functional nanomaterials into CA membranes significantly increased dye uptake. For instance, CA membranes loaded with graphene oxide and zeolite achieved 94.7% MB adsorption after 2 h under dark conditions (Fatiatun et al., 2025). While the adsorption capacity of CA/g-C_3N_4−2 is lower than that reported for these hybrid systems (Zhu et al., 2023), the key advantage of the present membranes lies in their dual functionality: efficient adsorption combined with high reusability and metal-free photocatalytic activity under visible light.

While advanced kinetic modeling can theoretically uncouple the precise simultaneous contributions of dynamic adsorption and photo-oxidation during the irradiation phase, the macroscopic phenomenological evidence presented here clearly validates the functional synergy: the membrane is not solely an adsorbent; its enhanced initial capacity directly accelerates surface reaction kinetics upon irradiation by minimizing the diffusion distance between the target pollutant and the short-lived reactive oxygen species.

3.7. Regeneration and sustainability

A major limitation of slurry-based photocatalysis is catalyst recovery. The CA/g-C_3N_4 membranes address this by enabling facile regeneration. Post-reaction membranes, which appeared blue due to adsorbed dye, were fully regenerated by simple visible-light exposure in a dry state (Fig. 8). Mechanistically, this dry regeneration is driven by the surface-confined photo-oxidation of the concentrated, adsorbed dye molecules. Upon visible-light excitation, the embedded g-C_3N_4 generates reactive oxygen species utilizing ambient oxygen and residual bound moisture, effectively degrading the retained pollutant without the mass-transfer barriers present in a bulk liquid phase. This light-driven regeneration protocol avoids the need for solvent cleaning or high-temperature treatments, aligning with the principles of green chemistry. The regenerated membranes were reused across five consecutive photocatalytic cycles to establish a baseline for operational stability. The system demonstrated a statistically negligible loss of activity, achieving 97.2% MB degradation even after the fifth cycle (Fig. 9). These findings confirm that the CA/g-C_3N_4−2 membranes not only withstand repeated use but also maintain almost their full photocatalytic potential after each regeneration step. While these initial five cycles serve as a standard metric to robustly validate the proof-of-concept for the material's structural integrity against leaching, extended operational studies beyond this threshold will naturally be required to fully define its industrial lifespan. This performance underscores their robustness and practical value for sustainable water treatment.

A comparison of the present results with literature reports further highlights the significance of regeneration in maintaining photocatalytic efficiency (Table 1). Although the CA/g-C_3N_4 membranes exhibited longer degradation times (240 min) compared to other polymeric membranes incorporating metal-based photocatalysts, several critical advantages distinguish this system. First, g-C_3N_4 is a metal-free photocatalyst that is considered environmentally safe, eliminating the risks of secondary metal ion contamination commonly associated with TiO_2, ZnO, or Cd-based nanomaterials (Drdanová et al., 2024; Swetha et al., 2025). Second, the process operates under visible light, in contrast to most reported systems that require energy-intensive UV irradiation. This attribute not only reduces operational costs but also enhances compatibility with natural sunlight, further aligning the system with sustainable water treatment practices.

4. Conclusion

This work establishes a scalable pathway for fabricating fully organic, metal-free photocatalytic membranes capable of efficient wastewater remediation under visible light. By integrating graphitic carbon nitride (g-C_3N_4) nanosheets into electrospun CA nanofibers, we successfully overcame the intrinsic limitations of powdered photocatalysts, specifically aggregation and difficult recovery, while leveraging the processability of renewable biopolymers.

Structural and chemical analyses revealed that the electrospinning process induces a favorable architecture. The resulting membranes exhibit a hierarchical porosity that maximizes light harvesting and mass transfer, superior to conventional phase-inversion counterparts. Furthermore, FTIR analysis evidenced a specific electronic perturbation and lattice rigidification of the g-C_3N_4 within the polymer matrix, suggesting an intimate interfacial coupling that facilitates charge separation rather than simple physical entrapment.

Under visible-light irradiation, the optimized CA/g-C_3N_4−2 membranes achieved 98.7% degradation of methylene blue at pH 10, driven primarily by a reductive mechanism involving superoxide radicals ($\bullet O_2^-$). Notably, the system maintained high efficiency across a broad alkaline window (pH 8–10), minimizing the need for strict pH regulation in industrial scenarios. Beyond degradation kinetics, the membranes demonstrated exceptional operational stability, retaining $>$ 97% efficiency after five consecutive regeneration cycles using a chemical-free, light-driven cleaning protocol.

CRediT authorship contribution statement

Edward Hermosilla: Writing – original draft, Supervision, Methodology, Investigation, Funding acquisition, Conceptualization. **Olga Rubilar:** Writing – review & editing, Supervision, Funding acquisition, Conceptualization. **Andrés Quiroz:** Writing – review & editing, Formal analysis. **Riquelme Pablo:** Investigation, Formal analysis. **Jeyson Hermosilla:** Validation, Investigation, Data curation. **Ana Obreque:** Writing – review & editing, Methodology, Investigation, Formal analysis. **María Cristina Diez:** Validation, Investigation, Formal analysis. **Marcela Diaz:** Resources, Methodology, Data curation. **Francisca Acevedo:** Validation, Investigation, Formal analysis.

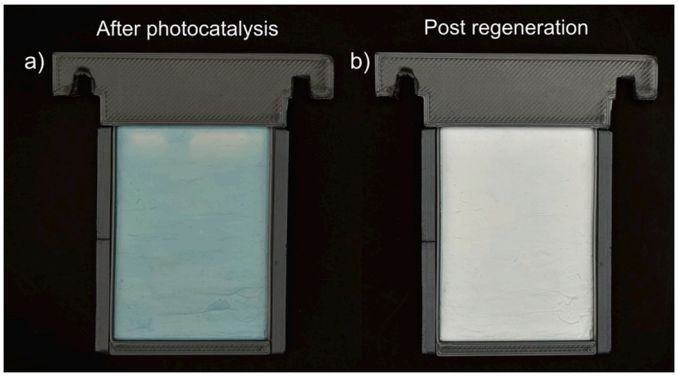

Fig. 8. Photographic images of the CA/g-C_3N_4−2 membrane: (a) after photocatalytic treatment and (b) following 1 h of regeneration under LED irradiation.

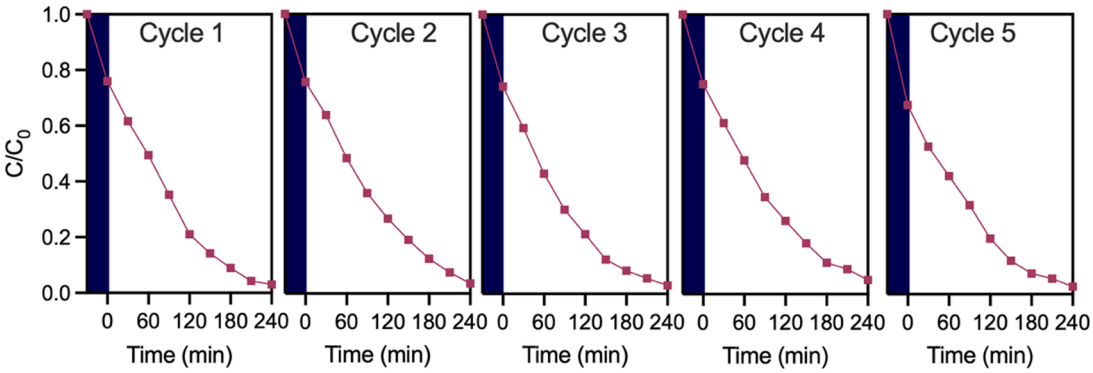

Fig. 9. Reusability performance of CA/g-C_3N_4 membranes over consecutive photocatalytic degradation cycles of MB.

Declaration of Competing Interest

The authors declare that they have no known competing financial interests or personal relationships that could have appeared to influence the work reported in this paper.

Acknowledgments

The authors gratefully acknowledge financial support from the National Agency for Research and Development (ANID), Chile, through projects FONDECYT 1250761, FONDECYT Iniciación 11230939, FONDAP 1523A0001, and Millennium Nucleus Bioproducts, Genomics and Environmental Microbiology – BioGEM (ANID-Milenio-NCN2023_054).

Appendix A. Supporting information

Supplementary data associated with this article can be found in the online version at doi:10.1016/j.eti.2026.105120.

Data availability

Data will be made available on request.

References

Abu-Dalo, M.A., Al-Rosan, S.A., Albiss, B.A., 2021. Photocatalytic degradation of methylene blue using polymeric membranes based on cellulose acetate impregnated with zno nanostructures. Polymers 13. https://doi.org/10.3390/polym13193451.

Ahmadi, S., Martinez Quimbayo, J., Beri, V., Yaah, K., Botelho De Oliveira, S., Ojala, S., 2025. A critical review on combining adsorption and photocatalysis in composite materials for pharmaceutical removal: Pros and cons, scalability, TRL, and sustainability. https://doi.org/10.1016/j.nexus.2025.100396.

Ahmadian, A., Ahmadi, S., Goharrizi, B.A., 2023. Roles of reactive species in photocatalysis: effect of scavengers and inorganic ions on dye removal from wastewater. Int. J. Environ. Sci. Technol. 20. https://doi.org/10.1007/s13762-023-04908-7.

Alizadeh, T., Nayeri, S., Hamidi, N., 2019. Graphitic carbon nitride (g-C 3 N 4)/graphite nanocomposite as an extraordinarily sensitive sensor for sub-micromolar detection of oxalic acid in biological samples. https://doi.org/10.1039/c9ra00982e.

Aljawrneh, B., Alsaad, A., Albiss, B., Alrousan, S., Alshanableh, A., Mutlaq, S., 2022. Cellulose acetate membranes treated with titanium dioxide and cerium dioxide nanoparticles and their nanocomposites for enhanced photocatalytic degradation activity of methylene blue. J. Mater. Sci. Mater. Electron. 33. https://doi.org/10.1007/s10854-022-08115-x.

Ashwini, M.A., Sagadevan, S., Fatimah, I., Paiman, S., Upadhyay, S., Garg, S., Johan, M.R., 2025. Photocatalytic performance of TiO2/g-C3N4 nanocomposite modified with carbon quantum dots for effective dye degradation: Experiments and DFT studies. J. Alloy. Compd. 1025, 180296. https://doi.org/10.1016/J.JALLCOM.2025.180296.

Asiri, A.M., Pugliese, V., Petrosino, F., Khan, S.B., Alamry, K.A., Alfifi, S.Y., Marwani, H.M., Alotaibi, M.M., Mukherjee, D., Chakraborty, S., 2022. Photocatalytic degradation of textile dye on blended cellulose acetate membranes. Polymers 14. https://doi.org/10.3390/polym14030636.

Attari, N., Hausler, R., 2020. Morphological investigation of cellulose acetate nanofibrous membranes. https://doi.org/10.11159/rtese20.124.

Behera, D., Mishra, P.P., Pattnaik, S.S., Das, N., Kumar, J., Behera, A.K., 2025. Sustainable removal of malachite green using cellulose extracted from waste bamboo culm sheath. RSC Sustain. 3, 4583–4597. https://doi.org/10.1039/d5su00133a.

Borban, B., Gohain, M.B., Yadav, D., Karki, S., Ingole, P.G., 2023. Nano-electrospun membranes: Green solutions for diverse industrial needs. J. Hazard. Mater. Adv. 12, 100373. https://doi.org/10.1016/J.HAZADV.2023.100373.

Boulkhessaim, S., Gacem, A., Khan, S.H., Amari, A., Yadav, V.K., Harharah, H.N., Elkhaleefa, A.M., Yadav, K.K., Rather, S.U., Ahn, H.J., Jeon, B.H., 2022. Emerging trends in the remediation of persistent organic pollutants using nanomaterials and related processes: a review. Nanomaterials 12, 2148. https://doi.org/10.3390/NANO12132148.

Buzga, M., MacHytka, E., Dvoracková, E., Švagera, Z., Stejskal, D., Máca, J., Král, J., 2022. Methylene blue: a controversial diagnostic acid and medication? Toxicol. Res. 11, 711. https://doi.org/10.1093/TOXRES/TFAC050.

Deogaonkar-Baride, S., Koli, M., Ghuge, S.P., 2025. Recycling textile dyeing effluent through ozonation: an environmentally sustainable approach for reducing freshwater and chemical consumption and lowering operational costs. J. Clean. Prod. 510. https://doi.org/10.1016/j.jclepro.2025.145641.

Drdanová, A.P., Krajčovičová, T.E., Gál, M., Nemčeková, K., Imreová, Z., Ryba, J., Naumowicz, M., Homola, T., Mackuľak, T., Svitková, V., 2024. Unveiling versatile applications and toxicity considerations of graphitic carbon nitride, 25, 7634 Int. J. Mol. Sci. 25, 7634. https://doi.org/10.3390/IJMS25147634.

El-Barbary, G., Ahmed, M.K., El-Desoky, M.M., Al-Enizi, A.M., Alothman, A.A., Alotaibi, A.M., Nafady, A., 2021. Cellulose acetate nanofibers embedded with Ag nanoparticles/CdSe/graphene oxide composite for degradation of methylene blue. Synth. Met. 278. https://doi.org/10.1016/j.synthmet.2021.116824.

Ennasraoui, B., Rhaya, M., Malekshah, R.E., Miyah, Y., Alahiane, S., Ouachtak, H., Jada, A., Addi, A.A., 2026. A novel dual-Z-scheme g-C3N4/BiOCl/Ag2WO4 heterojunction engineered for sunlight-driven photocatalytic degradation of methylene blue and amoxicillin. J. Photochem. Photobiol. A Chem. 471, 116671. https://doi.org/10.1016/J.JPHOTOCHEM.2025.116671.

Fatiatun, Bakar, Mohamed, S.A., Kusuma, A., Muqoyyanah, H.H., Mohamat, R., Kumar, V.V., Ali, K., Nuryadi, R., Azis, M.N.A., Ahmad, M.K., Mamat, M.H., Othman, M.H.D., 2025. High methylene blue adsorption efficiency of cellulose acetate-based electrospun nanofiber membranes modified with graphene oxide and zeolite. Int. J. Environ. Res. 19. https://doi.org/10.1007/s41742-024-00683-6.

González, S., Jaramillo-Fierro, X., 2025. Density functional theory study of methylene blue demethylation as a key step in degradation mediated by reactive oxygen species. Int. J. Mol. Sci. 26. https://doi.org/10.3390/ijms26041756.

Guo, M., Hu, Y., Wang, R., Yu, H., Sun, L., 2021. Molecularly imprinted polymer-based photocatalyst for highly selective degradation of methylene blue. Environ. Res. 194, 110684. https://doi.org/10.1016/j.envres.2020.110684.

Hassaan, M.A., El-Nemr, M.A., Elkatory, M.R., Ragab, S., Niculescu, V.C., El Nemr, A., 2023. Principles of photocatalysts and their different applications: a review. Top. Curr. Chem. https://doi.org/10.1007/s41061-023-00444-7.

Islam, T., Repon, M.R., Islam, Tarikul, Sarwar, Z., Rahman, M.M., 2023. Impact of textile dyes on health and ecosystem: a review of structure, causes, and potential solutions. Environ. Sci. Pollut. Res. https://doi.org/10.1007/s11356-022-24398-3.

Islam, M.D., Uddin, F.J., Rashid, T.U., Shahruzzaman, M., 2023. Cellulose acetate-based membrane for wastewater treatment—a state-of-the-art review. Mater. Adv. https://doi.org/10.1039/d3ma00255a.

Jiang, Z., Zhang, X., Wang, J., Chen, L., Chen, H.S., Yang, P., 2018. Ultrastable g-C3N4 assemblies with high quantum yield and reversible photoluminescence. Chem. Commun. 54, 13519–13522. https://doi.org/10.1039/C8CC07833E.

Kalaitzidou, K., Merachtsaki, D., 2023. Post-use recovery of nanoparticles. RSC Nanosci. Nanotechnol. 61, 120–143. https://doi.org/10.1039/BK9781837670215-00120.

Madankar, R., Umekar, M., Bhusari, G., Mondal, A., Raish, M., Afzal, M., Norek, M., Chaudhary, R., 2025. Rapid synthesis of graphitic carbon nitride nanosheets as an efficient adsorbent for removal of methylene blue and rhodamine B from aqueous solutions. Sci. Rep. 15, 1–21. https://doi.org/10.1038/S41598-025-13645-5;SUBJMETA=301,638,639;KWRD=CHEMISTRY,MATERIALS+SCIENCE.

Manea, L.R., Hristian, L., Leon, A.L., Popa, A., 2016. Recent advances of basic materials to obtain electrospun polymeric nanofibers for medical applications. IOP Conf. Ser. Mater. Sci. Eng. 145, 032006. https://doi.org/10.1088/1757-899X/145/3/032006.

Mishra, P.P., Behera, D., Suman, S., Das, N., Tripathy, B.C., Kumar, J., Behera, A.K., 2025. Synergistic efficiency of modified banana leaf derived cellulose-g-C3N4 hybrid composite: a sustainable approach for visible-light-driven photodegradation of dyes. RSC Adv. 15, 13712–13727. https://doi.org/10.1039/d5ra01156f.

Mishra, P.P., Mohanty, C., Behera, A.K., Das, R., Das, N., 2026a. Unfolding photo-degradation/reduction activity of heterojunction-derived g-C3N4/Sm2O3 for sustainable remediation of antibiotics and organic pollutants. J. Rare Earths 44, 1073–1084. https://doi.org/10.1016/j.jre.2025.06.020.

Mishra, P.P., Mohanty, C., Das, N., Mishra, M., Mohanty, A.K., Manna, S., Behera, A.K., 2024. Unlocking green solutions: cellulose as a lucrative heavy metal adsorbent in wastewater treatment-a comprehensive review. Water Air Soil. Pollut. 235. https://doi.org/10.1007/s11270-024-07636-x.

Mishra, P.P., Nanda, D., Sahoo, S., Das, N., Manna, S., Behera, A.K., 2026b. Architecting the Z-scheme heterojunction derived g-C3N4/Gd2O3 composite for visible-light mediated photocatalytic degradation of Ciprofloxacin and Tetracycline. J. Ind. Eng. Chem. 158, 574–584. https://doi.org/10.1016/j.jiec.2025.11.032.

Mohanty, C., Samal, A., Kumar, J., Behera, A.K., Das, R., Das, N., 2025. Design and first-principles investigation of step-scheme (S-scheme) g-C3N4/α-MnO2 nanojunction for polystyrene photoreforming into value-added chemicals and hydrogen. Int. J. Hydrog. Energy 120, 628–641. https://doi.org/10.1016/j.ijhydene.2025.03.193.

Molaei, M.J., 2023. Graphitic carbon nitride (g-C3N4) synthesis and heterostructures, principles, mechanisms, and recent advances: a critical review. Int. J. Hydrog. Energy 48, 32708–32728. https://doi.org/10.1016/J.IJHYDENE.2023.05.066.

Neukirch, F., Dreier, T., Priebe, H., Seitz, H., 2024. Investigation of cellulose acetate nanofibers using a DMSO based solvent system. Trans. Addit. Manuf. Meets Med. Trans. AMMM 6. https://doi.org/10.18416/AMMM.2024.24091848.

Niu, P., Dai, J., Zhi, X., Xia, Z., Wang, S., Li, L., 2021. Photocatalytic overall water splitting by graphitic carbon nitride. InfoMat 3, 931–961. https://doi.org/10.1002/INF2.12219.

Pellegrino, F., Pellutiè, L., Sordello, F., Minero, C., Ortel, E., Hodoroaba, V.D., Maurino, V., 2017. Influence of agglomeration and aggregation on the photocatalytic activity of TiO2 nanoparticles. Appl. Catal. B 216, 80–87. https://doi.org/10.1016/J.APCATB.2017.05.046.

Phakathi, N.A., Tichapondwa, S.M., Chirwa, E.M.N., 2025. Enhanced photodegradation of tetracycline by novel porous g-C3N4 nanosheets under visible light irradiation. J. Photochem. Photobiol. A Chem. 462, 116252. https://doi.org/10.1016/J.JPHOTOCHEM.2024.116252.

Pincheira, P.I.R., Gonçalves, I.M., Rubilar, O., Obreque, A., Hermosilla, E., Carvalho, A.J.A., Menezes, L., de, S., 2025. Graphitic carbon nitride nanosheets as scatterers for random laser action. Nanoscale 17, 20476–20487. https://doi.org/10.1039/D5NR02462E.

Prabu, G.T.V., Guruprasad, R., Sundaramoorthy, C., Vigneshwaran, N., 2022. Process optimization and modelling the BET surface area of electrospun cellulose acetate nanofibres using response surface methodology, 45 Bull. Mater. Sci. 45 (3), 133. https://doi.org/10.1007/S12034-022-02712-6.

Raj, S., Singh, H., Bhattacharya, J., 2023. Treatment of textile industry wastewater based on coagulation-flocculation aided sedimentation followed by adsorption: process studies in an industrial ecology concept. Sci. Total. Environ. 857. https://doi.org/10.1016/j.scitotenv.2022.159464.

Sabzehmeidani, M.M., Ghaedi, M., Karimi, H., 2021. Photocatalytic activity based on electrospun nanofibers. Interface Sci. Technol. 32, 625–672. https://doi.org/10.1016/B978-0-12-818806-4.00014-0.

Salehi, G., Bagherzadeh, M., Abazari, R., Hajilo, M., Taherinia, D., 2024. Visible light-driven photocatalytic degradation of methylene blue dye using a highly efficient Mg-Al LDH@g-C3N4@Ag3PO4 nanocomposite. ACS Omega 9, 4581–4593. https://doi.org/10.1021/ACSOMEGA.3C07326/ASSET/IMAGES/LARGE/AO3C07326_0012.JPEG.

Sasikala, V., Karthik, P., Ravichandran, S., Prakash, N., Rajesh, J., Mukkannan, A., 2024. Facile synthesis of BiOCl incorporated polymer membrane for effective photocatalytic dye degradation. J. Polym. Environ. 32, 1937–1951. https://doi.org/10.1007/s10924-023-03096-2.

Shakoor, M.H., Shakoor, M.B., Jilani, A., Ahmed, T., Rizwan, M., Dustgeer, M.R., Iqbal, J., Zahid, M., Yong, J.W.H., 2024. Enhancing the photocatalytic degradation of methylene blue with graphene oxide-encapsulated g-C3N4/ZnO ternary composites. ACS Omega 9, 16187–16195. https://doi.org/10.1021/ACSOMEGA.3C10172/ASSET/IMAGES/LARGE/AO3C10172_0007.JPEG.

Solayman, H.M., Yahya, N.Y., Leong, K.-H., Hossain, Md.K., Kang, K., Sim, L.C., Zoh, K.-D., Khan, Md.B., Abd Aziz, A., 2024. Photocatalytic performance of acid exfoliated graphitic carbon nitride (G-C3n4) for the degradation of dye under direct sunlight. https://doi.org/10.2139/SSRN.4952591.

Song, R., Yao, L., Sun, C., Yu, D., Lin, H., Li, G., Lian, Z., Zhuang, S., Zhang, D., 2023. Electrospun membranes anchored with g-C3N4/MoS2 for highly efficient photocatalytic degradation of aflatoxin B1 under visible light. Toxins 15, 133. https://doi.org/10.3390/TOXINS15020133/S1.

Swetha, K., Bhatnagar, A., Lakavathu, M., Poornima, P., Ganesh, P., Kamath, A., Bonam, S.R., Srinivasula, S.M., Kurapati, R., 2025. Biological degradation of graphitic carbon nitride sheets and autophagy induction in macrophages. Nanoscale 17, 15267–15278. https://doi.org/10.1039/D5NR00795J.

Tian, G., Duan, C., Che, S., Zhao, B., Zhou, B., Ni, Y., 2025. Facile fabrication of a cellulose-based photocatalytic membrane decorated with core-shell heterojunction microspheres for efficient and continuous wastewater remediation. Sep. Purif. Technol. 354. https://doi.org/10.1016/j.seppur.2024.129183.

Vera, J., Herrera, W., Hermosilla, E., Schalchli, H., Díaz, R., Fincheira, P., Seabra, A.B., Quiroz, A., Tortella, G., Rubilar, O., 2025. Photodegradation of lignin biowaste catalyzed by biosynthesized zinc oxide nanoparticles using the leaf extract of Aristotelia chilensis. Results Eng. 25, 103866. https://doi.org/10.1016/J.RINENG.2024.103866.

Wang, L., Wang, Yinggang, Wang, Yun, Wang, H., Wu, H., Gao, D., 2024. Efficient photocatalytic degradation of sulfonamides in wastewater using g-C3N4 heterostructures: a critical review. Environ. Technol. Innov. 36, 103854. https://doi.org/10.1016/J.ETI.2024.103854.

Yang, X., Zhang, L., Wang, D., Zhang, Q., Zeng, J., Zhang, R., 2021. Facile synthesis of nitrogen-defective g-C3N4 for superior photocatalytic degradation of rhodamine B. RSC Adv. 11, 30503–30509. https://doi.org/10.1039/D1RA05535F.

Zhang, T., Oyama, T., Horikoshi, S., Hidaka, H., Zhao, J., Serpone, N., 2002. Photocatalyzed N-demethylation and degradation of methylene blue in titania dispersions exposed to concentrated sunlight. Sol. Energy Mater. & Sol. Cells.

Zhang, S., Su, C., Ren, H., Li, M., Zhu, L., Ge, S., Wang, M., Zhang, Z., Li, L., Cao, X., 2019. In-situ fabrication of g-c3n4/zno nanocomposites for photocatalytic degradation of methylene blue: synthesis procedure does matter. Nanomaterials 9. https://doi.org/10.3390/nano9020215.

Zhang, D., Zhang, X., Gao, Y., Xu, J., Huang, H., Xiong, X., Wu, H., Xiong, W., Zhang, C., 2025. A novel recyclable g-C3N4/calcite/pumice floating photocatalyst for effective inactivation of microcystis aeruginosa under visible light irradiation. Chem. Eng. J. 523. https://doi.org/10.1016/j.cej.2025.168476.

Zhang, C., Zhang, X., Yuan, C., Huang, H., Xiong, X., Wu, H., Wang, D., 2024. Efficient simultaneous removal of phosphate and microcystin-LR in water using a novel g-C3N4/calcite composite under dark-visible light cycles. Chem. Eng. J. 499. https://doi.org/10.1016/j.cej.2024.156490.

Zheng, H., Lu, H., Li, S., Niu, J., Leong, Y.K., Zhang, W., Lee, D.J., Chang, J.S., 2024. Recent advances in electrospinning-nanofiber materials used in advanced oxidation processes for pollutant degradation. Environ. Pollut. 344, 123223. https://doi.org/10.1016/J.ENVPOL.2023.123223.

Zhu, W., Wu, Z., Zhao, S., Lv, F., Zhang, Y., Guo, S., 2023. Selective adsorption and separation of methylene blue from wastewater by self-standing polyvinylpyrrolidone and SiO2 electrospun membranes. Chem. Eng. Sci. 280, 119009. https://doi.org/10.1016/J.CES.2023.119009.

Zhuang, H., Cai, Z., Xu, W., Huang, M., Liu, X., 2019. situ construction of WO3/g-C3N4 composite photocatalyst with 2D–2D heterostructure for enhanced visible light photocatalytic performance. New. J. Chem. 43, 17416–17422. https://doi.org/10.1039/C9NJ04311J.